

Coherent manipulation of interacting electron qubits on solid neon

Xinhao Li,^{1,2, a)} Yizhong Huang,^{2,3} Xu Han,^{2,3} Xianjing Zhou,^{4,5, b)} Amir Yacoby,¹ and Dafei Jin^{6, c)}

¹⁾Department of Physics, Harvard University, Cambridge, Massachusetts 02138, USA

²⁾Center for Nanoscale Materials, Argonne National Laboratory, Lemont, Illinois 60439, USA

³⁾Pritzker School of Molecular Engineering, University of Chicago, Chicago, Illinois 60637, USA

⁴⁾National High Magnetic Field Laboratory, Tallahassee, Florida 32310, USA

⁵⁾Department of Mechanical Engineering, FAMU-FSU College of Engineering, Florida State University, Tallahassee, Florida 32310, USA

⁶⁾Department of Physics and Astronomy, University of Notre Dame, Notre Dame, Indiana 46556, USA

(Dated: 26 August 2025)

Solid neon has recently emerged as a pristine material host for electron qubits. Single electron-on-solid-neon (eNe) charge qubits have shown extraordinarily long coherence times and high operation fidelities. Realizing two-qubit gates in this platform is the next major step for practical quantum information processing. In this work, we demonstrate frequency- and time-domain coherent manipulation of multiple eNe charge qubits that are coupled by charge-charge interactions. Cross-resonance and bSWAP two-qubit gates are implemented, laying the foundation for universal quantum computing. Inter-qubit coupling strength exceeding 60 MHz is observed, promising fast and high-fidelity two-qubit gates. These results highlight the potential to develop the eNe qubit platform into a compelling quantum computing architecture.

Electrons on solid neon (eNe) is an emerging solid-state qubit platform^{1–4}. Owing to the ultraclean environment provided by the noble-element neon, qubits based on the motional (charge) states of eNe have shown exceedingly long coherence². The inherent electrical addressability of charge states allows for straightforward control and readout by microwave photons in a circuit quantum electrodynamics architecture (cQED)^{5,6}, significantly simplifying the circuit design. The small footprint of eNe charge qubits offers another unique advantage for high-volume integration within quantum circuits. To further advance the eNe platform towards a useful quantum information architecture, it is essential to construct systems with multiple interacting qubits and achieve coherent manipulation of all these qubits^{4,7}. In our previous work, we observed two eNe charge qubits trapped around the same designed trapping area and coupled through microwave photons in a common superconducting resonator². Later theoretical and experimental studies show that an imperfect neon surface may play an important role in co-trapping multiple electrons^{8–10}. However, all our observed through-resonator inter-qubit couplings so far are not strong enough for coherent real-time two-qubit gate operations.

In this work, we achieve the first coherent manipulation of multiple interacting electron qubits on solid neon. The rough neon surface provides a natural

mechanism to pack several electrons at close distances with strong charge-charge interactions surpassing the qubits' decoherence rates^{4,11}. In a two-qubit system, spectroscopic measurements show an inter-qubit coupling strength of $J/2\pi = 3.35$ MHz. By driving one of the two qubits, which is strongly coupled with the superconducting resonator, we are able to demonstrate the cross-resonance and bSWAP types of all-microwave two-qubit gates¹². The experimental results match well the theoretical simulations based on measured parameters. Furthermore, we observe even stronger coupling in a three-qubit system, with a maximum inter-qubit coupling strength of $J/2\pi = 62.5$ MHz. These results lay the foundation for scalable quantum information processing with this emerging platform. The local charge-charge coupling between qubits on solid neon may also provide a unique testbed for quantum simulation of correlated many-electron systems in an ultrapure near-vacuum environment^{13,14}.

Multi-qubit systems

Multiple electron qubits can be trapped in the same trapping area on our device, as shown in Fig. 1A. They can be driven and read out through microwave photons in the resonator. The electron-photon coupling strength is determined by the magnitude and alignment between the electric dipole moments of the qubits and the local electric field of the microwave photons. For two closely arranged qubits, Q_i and Q_j , they can couple through not only microwave photons but also direct charge-charge interactions. The system Hamiltonian can be written as

$$\hat{H}_{\text{sys}} = \hat{H}_{\text{r}} + \hat{H}_{\text{q}} + \hat{H}_{\text{r-q}} + \hat{H}_{\text{q-q}}, \quad (1)$$

where the resonator Hamiltonian \hat{H}_{r} , the qubit Hamiltonian \hat{H}_{q} , the resonator-qubit interaction Hamiltonian $\hat{H}_{\text{r-q}}$, and the qubit-qubit direct interaction Hamiltonian $\hat{H}_{\text{q-q}}$ are

$$\hat{H}_{\text{r}} = \hbar\omega_{\text{r}}\hat{a}^{\dagger}\hat{a}, \quad (2)$$

$$\hat{H}_{\text{q}} = \sum_i \frac{1}{2}\hbar\omega_i\hat{\sigma}_i^z, \quad (3)$$

$$\hat{H}_{\text{r-q}} = \sum_i \hbar g_i(\hat{a}^{\dagger}\hat{\sigma}_i^- + \hat{a}\hat{\sigma}_i^+), \quad (4)$$

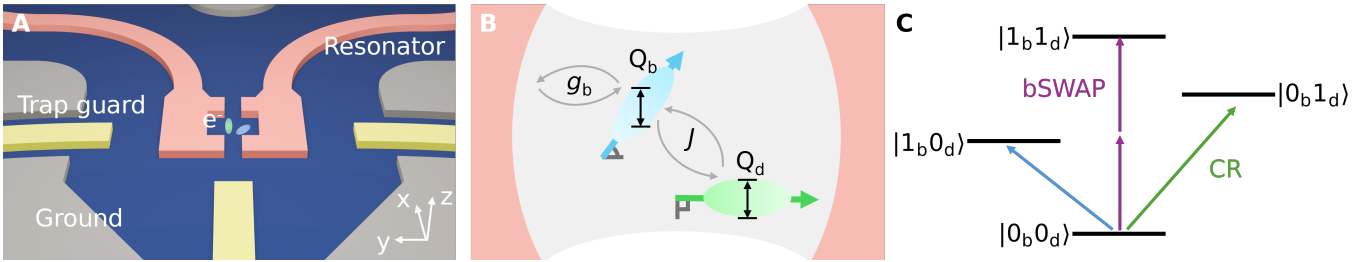


Fig. 1. Schematic of multi-qubit coupling on neon-covered superconducting resonator. (A) Two closely arranged qubits trapped at the open end of a splitting co-planar waveguide superconducting resonator (pink), surrounded by electrical gates (yellow). The blue and gray structures are the intrinsic silicon substrate and ground, respectively. In the experiment, varying gate voltage is symmetrically applied on the left and right trap guards (ΔV_{tg}) or on the resonator pins (ΔV_{res}) to tune the qubits' transition frequency. (B) Schematic of the interactions between a two-qubit system and the superconducting resonator, where a bright qubit Q_b and a dark qubit Q_d are coupled with strength J and Q_b is coupled to the resonator with strength g_b . Due to the orthogonal dipole alignment to the field, Q_d is invisible to the resonator. (C) Energy level schematic of the two-qubit system showing possible transitions.

and

$$\hat{H}_{q-q} = \sum_{ij} \hbar J_{ij} (\hat{\sigma}_i^+ \hat{\sigma}_j^- + \hat{\sigma}_i^- \hat{\sigma}_j^+) \quad (5)$$

Here, ω_r is the resonator frequency, ω_i is the transition frequency of Q_i , g_i is the coupling strength between the resonator and Q_i , \hat{a} and \hat{a}^\dagger are the annihilation and creation operators of resonator photons, $\hat{\sigma}_i^z$, $\hat{\sigma}_i^-$, and $\hat{\sigma}_i^+$ are the Pauli- z , lowering, and raising operators acting on Q_i . J_{ij} represents the transverse inter-qubit coupling strength between Q_i and Q_j (ref. ¹²). In the following section, we show that the experimentally observed longitudinal (ZZ) coupling strength is small in the system, so we exclude it from the system Hamiltonian model ^{11,15}.

The imperfect neon surface can pack two electrons at a close distance but with distinct dipole orientations that lead to different electron-photon (qubit-resonator) coupling strengths ^{5,16}. As shown in Fig. 1B, inside a two-qubit coupled system, one of the qubits with a dipole moment orthogonal to the microwave (MW) electric field of a superconducting resonator can result in a near-zero qubit-resonator coupling strength and negligible dispersive shift of the resonator spectrum. We may call it the “dark” qubit Q_d . The other qubit with a dipole moment significantly aligned to the MW electric field has a coupling strength g_b . Its quantum states can then be dispersively read out. We call it the “bright” qubit Q_b . In such a case, we have a system Hamiltonian with $g_d \sim 0$ and a finite J between Q_b and Q_d (ref. ¹⁷).

This two-qubit system can support all-microwave-driven two-qubit operations, including the cross-resonance (CR) and bSWAP types of two-qubit gates, as shown in Fig. 1C. All-microwave two-qubit gates are widely used for fixed-frequency qubits thanks to their easy implementation, which also preserves qubit coherence by avoiding electrostatic and flux gating ¹². For the CR gate, Q_d is excited by driving Q_b at the frequency of Q_d , generating the transition $|0_b0_d\rangle \rightarrow |0_b1_d\rangle$

(refs. ^{18–20}). For the bSWAP gate, Q_b and Q_d are driven monochromatically through a two-photon process near the frequency middle point between the two, generating the transition $|0_b0_d\rangle \rightarrow |1_b1_d\rangle$ (refs. ^{17,21}).

Two-qubit spectroscopy

We have achieved the strong coupling between the two eNe qubits. Figure 2A shows the two-tone qubit spectroscopy measurement. We drive the system with a continuous-wave (CW) tone at a variable frequency, and probe the system with another CW tone at the fixed resonator frequency, with a low power, approximately -130 dBm reaching the resonator's input coupler. Two clear avoided crossings are observed while tuning the bias voltage on the trap guard electrode (ΔV_{tg}). The splitting magnitude of $J/2\pi = 3.35$ MHz is larger than the linewidth of the hybrid states above and below the splitting, as shown in Fig. 2B. This indicates the strong coupling between the “bright” qubit (Q_b) and “dark” qubit (Q_d).

Individually, the bright Q_b has a hyperbolic frequency dependence on ΔV_{tg} , with a charge sweet spot (SS) located near 5.71 GHz, which is about 40 MHz above the resonator frequency at 5.668 GHz. The coupling between Q_b and the resonator dispersively pushes the resonator spectrum, especially when Q_b is tuned to its SS frequency (fig. S1). Based on this, we estimate the coupling strength between Q_b and the resonator to be $g_b/2\pi = 3.76$ MHz.

In contrast, the interaction between the dark Q_d and the superconducting resonator is much weaker than that of Q_b . Meanwhile, the secondary shift of the resonator caused by the dispersive push of Q_d on Q_b is also small. Together, these lead to a negligible Q_d -state-dependent shift of the resonator frequency and the absence of visible Q_d spectroscopy in Fig. 2A. In addition, the spectroscopic symmetry of the two avoided crossing in against ΔV_{tg} indicates that the frequency of the dark Q_d is much less sensitive to ΔV_{tg} compared to that for the bright Q_b ,

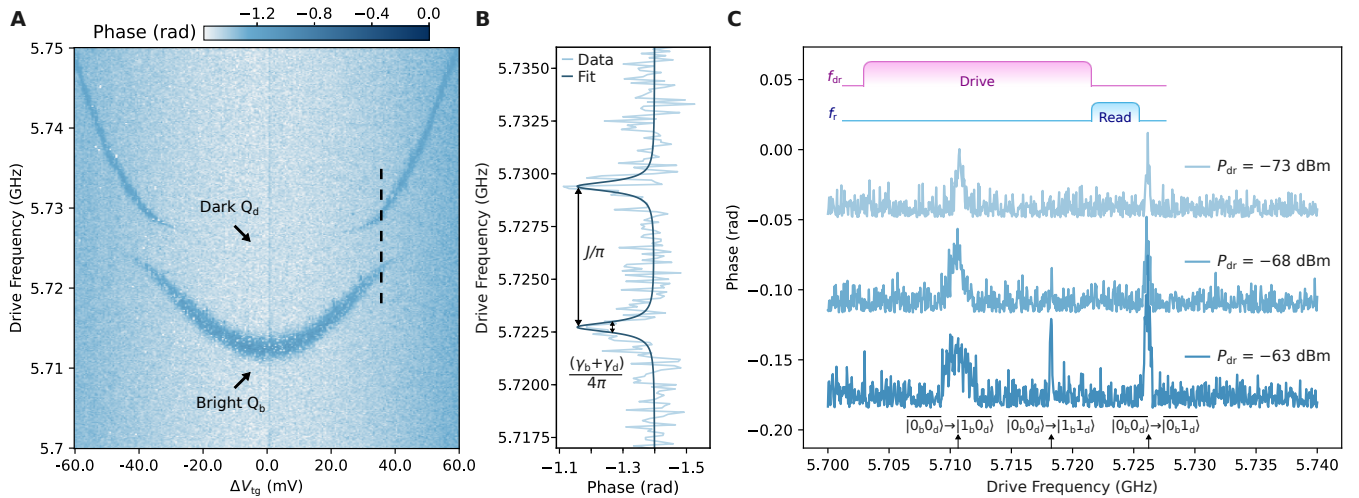


Fig. 2. Spectroscopic characterization of coherent two-qubit coupling on solid neon. (A) Two-tone qubit spectroscopy with avoided splittings. The arrows mark the bright qubit Q_b and the dark qubit Q_d . The dashed line marks the avoided crossing as in (B). (B) Line cut of the two dressed states at the avoided crossing with splitting magnitude of $J/2\pi = 3.35$ MHz. (C) Qubits spectroscopy measured with high-power pulsed readout. Driving pulses with varied frequency (f_{dr}) reach the resonator's input coupler with power (P_{dr}) increased from -73 dBm to -63 dBm, activating transitions corresponding to the CR and bSWAP two-qubit operations. The measurements were taken when the system was biased at $\Delta V_{tg} = 0$ V. The phase curves are off-set for visualization.

with a nearly constant frequency of 5.726 GHz in the voltage scanning range of Fig. 2A. These observations all suggest the misalignment between Q_d 's dipole and the microwave and direct current (DC) gating fields.

We attribute the two-qubit coupling to charge-charge interactions at short distances. The spectroscopic observations reveal a coupled two-qubit system represented in Fig. 1B, with a finite g_b but negligible g_d in Eq. 4. Due to the distinct coupling strengths of the two qubits individually with the resonator, we can rule out the case of virtual microwave photon exchange between the two qubits through the resonator, in which the inter-qubit exchange strength $J = g_b g_d (1/\Delta_b + 1/\Delta_d)/2$, where $\Delta_{b,d}$ are the detune between the qubits and the resonator²².

The dark Q_d can be probed by swapping its population to the bright Q_b . The swap operation can be realized using the ac-Stark shift of Q_b when the resonator is populated while probing the system with a readout pulse at the resonator frequency. Given the dispersive coupling strength of $\chi/2\pi \approx 0.33$ MHz, the ac-Stark effect will blue shift Q_b 's frequency by $2\bar{n}\chi$ (refs. 2,6), crossing Q_d 's frequency when the averaged intra-cavity photon number \bar{n} is approximately 20. Due to the undetectable coupling between Q_d and the resonator, the probe signal will not affect Q_d directly. With the increase of photon number in the cavity during the readout with sufficient probe power, Q_b 's frequency gradually crosses that of Q_d , resulting in the states swap and eventually the Q_d -state-dependent readout. This effect is turned off when the probe tone is weak, and the ac-Stark shift of Q_b is insufficient to cross the frequency of Q_d , as in the case of Fig. 2A. We simulate the pulsed readout process in ref. 23, with varied probe

power to illustrate the detailed swap process during a 700 ns readout pulse (fig. S2), as in the following experiments.

With this method, we perform pulsed qubit spectroscopy when biased at Q_b 's SS. A long square pulse (10 μ s) with a varying driving frequency f_{dr} and a driving power (P_{dr}) is first applied to drive the system to a specific state, followed by a short square probe pulse (700 ns) at the resonator frequency f_r with approximately -120 dBm power reaching the resonator. The pulse sequence is shown in the inset of Fig. 2C. At low driving power, we observe two transitions at 5.711 GHz and 5.726 GHz, corresponding to the frequencies of Q_b at its SS and Q_d . The appearance of $|0_b0_d\rangle \rightarrow |0_b1_d\rangle$ transition indicates that the long driving pulse pumps Q_d to a certain population, corresponding to the CR transition of a two-qubit coupled system^{18,20}, as shown in Fig. 1C. With an increasing driving power, we observe another transition peak ($|0_b0_d\rangle \rightarrow |1_b1_d\rangle$) near the middle of the Q_b and Q_d frequencies of 5.7185 GHz. This corresponds to the bSWAP type of two-qubit operation in Fig. 1C, involving two-photon excitation^{17,21}. The fact that $\omega_{|1_b1_d\rangle} - \omega_{|0_b1_d\rangle} - \omega_{|1_b0_d\rangle} \simeq 0$ suggests the effective longitudinal (ZZ) interaction in the system is negligible^{11,15}. In summary, through the frequency-domain characterization, we have observed the coherent coupling between two qubits on solid neon, which can support both the CR and the bSWAP types of two-qubit operation.

Two-qubit gate operations

Following the frequency-domain characterization of the coupled system, we perform time-domain two-

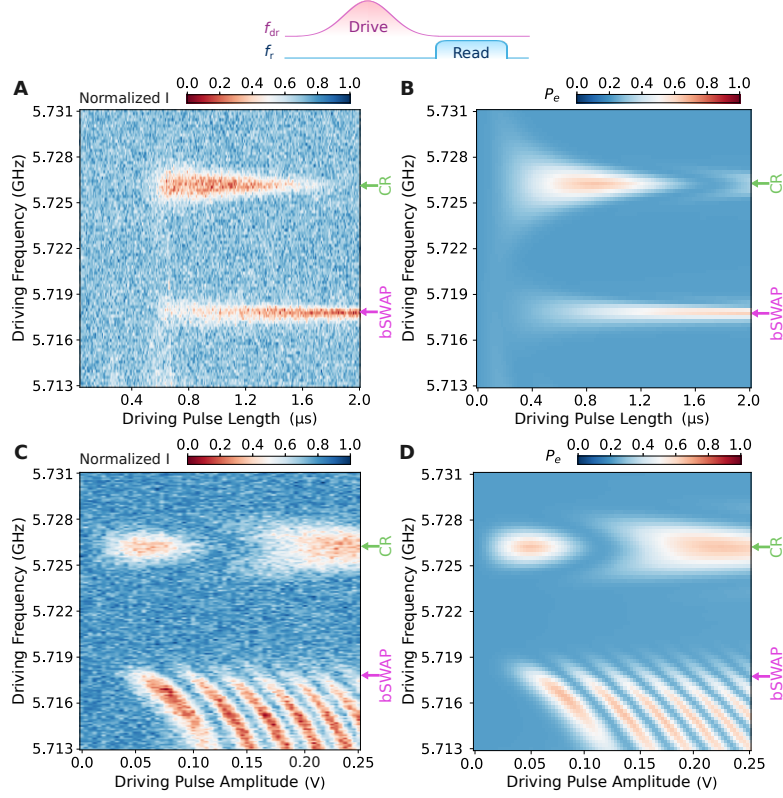


Fig. 3. Time-domain all-microwave two-qubit operations on solid neon. (A) and (C) Driving pulse length-frequency (A) and driving pulse amplitude-frequency (C) Rabi measurements, following the pulse sequences in the inset, showing the two operations corresponding to cross-resonance (CR, green arrows) and bSWAP (magenta arrows) two-qubit gates. (B) and (D) Simulated Q_b excited state population after the readout pulse in driving pulse length-frequency (B) and driving pulse amplitude-frequency (D) Rabi measurements.

qubit operations corresponding to the CR and bSWAP gates. Figure 3A plots the readout signal following Gaussian-shaped driving pulses with varying lengths and approximately -70 dBm reaching the resonator input coupler. The driving pulses are truncated at $\pm 2.5\sigma$ on each side, where σ is the standard deviation of the Gaussian envelope. The parameters of the readout pulses are the same as described in the last section. Two oscillation features corresponding to the CR operation near 5.726 GHz and the bSWAP operation near 5.718 GHz can be observed. Based on the system Hamiltonian, we numerically simulate the system evolution through the drive and readout process in the Rabi measurements^{23,24}. Figure 3B plots the simulated population of Q_b after readout. And the evolution of the two-qubit system through the driving process is shown in fig. S4. Thanks to the readout process, the excitation of Q_d via the two-qubit operation can be reflected in the Q_b population, as shown in Fig. 3B, and consequently, the recorded readout signal.

The simulated results match well with the experimental observations. For the CR operation (green arrows), Q_d was driven by pumping Q_b at the transition frequency of Q_d , whose excited state population

reached maximum when the pulse length was approximately $0.8\ \mu\text{s}$. Meanwhile, the CR operation barely excites Q_b , as shown in fig. S4. For the bSWAP operation (magenta arrows), the two-photon process drives the two qubits simultaneously, while the oscillation frequency is much lower than the CR operation. Under a square driving pulse with amplitude A , and negligible direct driving on the Q_d , the oscillation frequency induced by CR operation is $\Omega_{\text{CR}} = AJ/(\Delta_{\text{bd}} + 2J^2/\Delta_{\text{bd}})$ (ref. ¹⁸). For the bSWAP operation, the oscillation frequency is approximately $\Omega_{\text{bSWAP}} = 2AJ/(\Delta_{\text{bd}} + 2J^2/\Delta_{\text{bd}})^2$ (ref. ¹⁷), where Δ_{bd} is the frequency separation between Q_b and Q_d . When the bSWAP operation performs a π rotation, which is about $2\ \mu\text{s}$ in our case, it is locally equivalent to an iSWAP gate with appropriate single-qubit rotations¹⁷.

Furthermore, we performed driving pulse-amplitude-dependent Rabi oscillation measurement with a Gaussian-shaped driving pulse of $800\ \text{ns}$ length and output pulse amplitude varying from $0.0\ \text{V}$ to $0.25\ \text{V}$, corresponding to zero power to $-57\ \text{dBm}$ reaching the resonator input coupler. Again, we observe oscillating patterns near 5.726 GHz and 5.718 GHz, corresponding to the CR (green arrows) and bSWAP (magenta arrows)

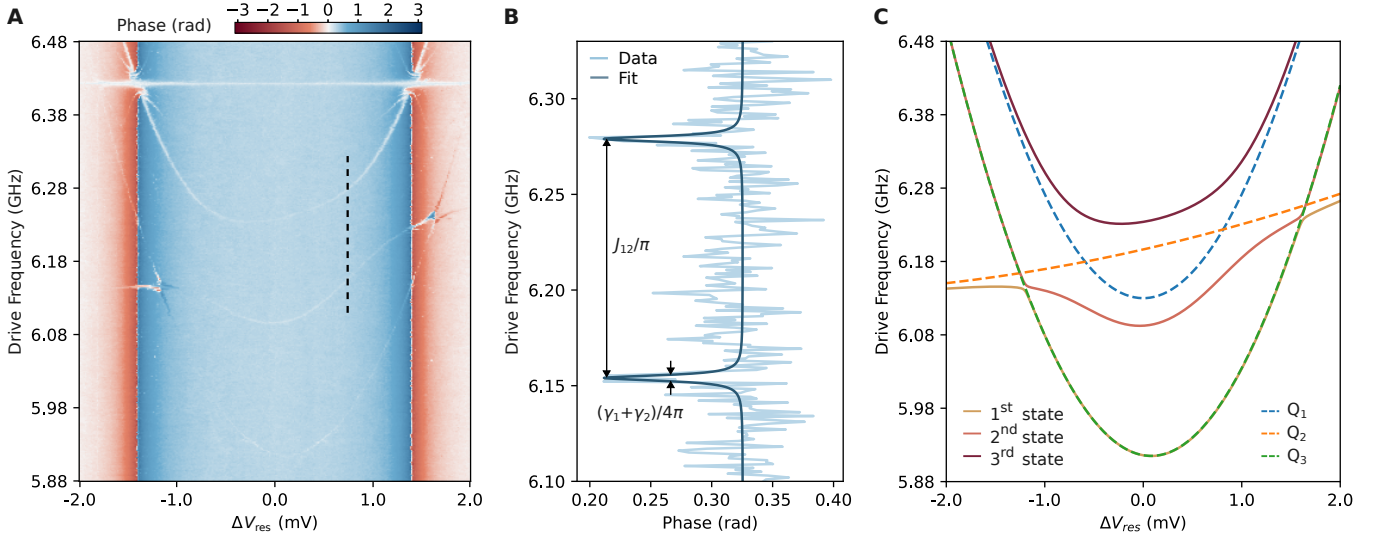


Fig. 4. Spectroscopic characterization of a three-qubit coupled system on solid neon. (A) Two-tone measured qubits spectroscopy showing the three-qubit coupled system. The dashed line marks the avoided crossing as in (B). (B) The line cut showing large coupling strength between Q_1 and Q_2 of $J_{12}/2\pi = 62.5 \text{ MHz}$. (C) Calculated eigenstate energy diagram of the three-qubit coupled system, with bare qubit states shown as dashed lines.

operations. We attribute the “waterfall-like” patterns in the frequency range 5.713 through 5.718 GHz in Fig. 3C to the effects of the Gaussian pulse shape and the ac-Stark shift of Q_b under higher driving power²³, which are reproduced by simulations in Fig. 3D and fig. S4.

These results demonstrate, for the first time, time-domain two-qubit operations in a eNe qubit platform, offering the potential for multi-qubit quantum processors based on charge qubits on solid neon. Further optimization of the two-qubit gate and readout is crucial to achieving high-fidelity operations.

Three-qubit strong coupling

We further realized a three-qubit system on solid neon with strong inter-qubit coupling. Figure 4A plots the two-tone measured qubit spectrum while varying the gate voltage on the resonator electrode (ΔV_{res}), revealing the energy diagram of this three-qubit system. One of them (Q_1) is directly coupled with a superconducting resonator, while the other two (Q_2 and Q_3) are serially coupled to Q_1 . Compared to Q_1 , the interactions strengths of Q_2 and Q_3 with the resonator are weak. We do not observe the vacuum Rabi splitting between them and the resonator. Besides, the dispersive phase shift of the resonator induced by Q_2 and Q_3 is also small when they are not hybridized with Q_1 .

In Fig. 4B, the line cut around $\Delta V_{\text{res}} = 0.74 \text{ mV}$ shows a coupling strength of $J_{12}/2\pi = 62.5 \text{ MHz}$ between Q_1 and Q_2 . On the other hand, the coupling strength $J_{23}/2\pi$ between Q_2 and Q_3 is much smaller, at approximately 5 MHz level. The difference in inter-qubit coupling strengths can be caused by the varied distance and dipole orientation between qubits. Besides, since Q_2 and Q_3

both weakly coupled with the resonator, probably due to unfavorable alignment between their dipole and the microwave field, we attribute the inter-qubit coupling in the three-qubit system to charge-charge interactions instead of virtual photon exchange.

Figure 4C shows the calculated eigenstates of the system, which match well with the two-tone spectroscopy. Q_1 and Q_2 ’s SS are both near 6.13 GHz, while Q_3 ’s SS is more detuned to approximately 5.91 GHz. All the three qubits are responsive to the bias voltage on the resonator electrode with various sensitivities. The parameters applied in the calculation is listed in tab. S2. Due to the large coupling strength between Q_1 and Q_2 , the state mixing of the three qubits results in the energy diagram of the coupled system, which deviates from the uncoupled qubit spectrum. As a result, the three mixed states are all visible in the two-tone measurement in Fig. 4A. These observations indicate the possibilities of simultaneously entangling more than two qubits in the eNe system that may be applied for small- to medium-scale quantum simulations^{13,14}.

Discussion and outlook

In this work, we have realized coherent manipulation of multiple electron qubits on solid neon mediated by charge-charge interactions. In a two-qubit system, frequency-domain spectroscopy shows strong inter-qubit coupling. While time-domain measurements demonstrate both cross-resonance and bSWAP two-qubit operations, paving the way for the optimization of high-fidelity two-qubit gates on solid neon. Further, a three-qubit system with over 60 MHz inter-qubit coupling strength shows the potential of building more complex systems with qubits on solid neon.

Charge-charge interactions between qubits at short distances may enable new possibilities for quantum information processing on solid neon. For the two systems studied in this work, qubits can acquire distinct coupling strengths with superconducting resonators. Utilizing such possibilities, qubits with dipole moments oriented normal to the resonator field can serve as quantum memories for nearby coupled qubits^{25,26}, or act as a quantum mediator²⁷. The variation in qubit-resonator coupling strengths further reflects the complexity of electron trapping on solid neon films and points to the important role of surface profile in determining qubit properties^{8–10,28}.

Establishing coherent charge interactions between adjacent qubits on solid neon is a crucial step in advancing this emerging solid-state qubit platform. Similarly, strong inter-qubit coupling has been demonstrated in semiconductor qubit dots through various interaction mechanisms at short distance^{29–33}. However, a multi-qubit system purely relying on local interactions will pose challenges to integrated control and readout circuits at large qubit volume. Entanglement between distant qubits through superconducting cavity buses could ease these limits posed by local interactions^{22,34–36}. High-impedance resonators made of high-kinetic inductance thin films^{37,38} and Josephson junction arrays^{39,40} have been applied to achieve coherent interactions between distant semiconductor qubits. Further improvements in the control of individual qubit properties above solid neon with refined film growth, electron trapping and gating mechanisms, as well as the development of a compatible high-impedance resonator^{41,42} would facilitate remote entanglements between distant qubits and hybridize it with other quantum platforms^{26,43}. Looking ahead, the integration of short- and long-distance interactions between qubits on solid neon could pave the way for an on-chip quantum network.

Data availability

The data that support the findings of this study are available from the corresponding authors upon request. Source data are provided with this paper.

Code availability

The codes used to perform the experiments and to analyze the data in this work are available from the corresponding authors upon request.

ACKNOWLEDGMENTS

D.J., A.Y., and X.L. acknowledge support from the Air Force Office of Scientific Research (AFOSR) under Award No. FA9550-23-1-0636 for device fabrication and simulation. D.J. acknowledges support from the Department of Energy (DOE) under Award No. DE-SC0025542 for material growth and characterization. D.J. acknowledges support from the National Science Foundation (NSF) under Award No. OSI-2426768 for

theoretical modeling. D.J., X.Z., and Y.H. acknowledge support from the Julian Schwinger Foundation for Physics Research for instrument development. X.H. acknowledges support from the U.S. DOE, Office of Science, Advanced Scientific Computing Research (ASCR) program under Contract No. DE-AC02-06CH11357 as part of the InterQnet quantum networking project. Work performed at the Center for Nanoscale Materials, a U.S. Department of Energy Office of Science User Facility, was supported by the U.S. DOE, Office of Basic Energy Sciences, under Contract No. DEAC02-06CH11357. The authors thank Xuedong Hu and David I. Schuster for helpful discussions.

^aEmail: xinhaoli@fas.harvard.edu

^bEmail: xianjing.zhou@fsu.edu

^cEmail: dfjin@nd.edu

¹X. Zhou, G. Koolstra, X. Zhang, G. Yang, X. Han, B. Dizdar, X. Li, R. Divan, W. Guo, K. W. Murch, *et al.*, “Single electrons on solid neon as a solid-state qubit platform,” *Nature* **605**, 46–50 (2022).

²X. Zhou, X. Li, Q. Chen, G. Koolstra, G. Yang, B. Dizdar, Y. Huang, C. S. Wang, X. Han, X. Zhang, *et al.*, “Electron charge qubit with 0.1 millisecond coherence time,” *Nature Physics* **20**, 116–122 (2024).

³W. Guo, D. Konstantinov, and D. Jin, “Quantum electronics on quantum liquids and solids,” *Progress in Quantum Electronics* **99**, 100552 (2024).

⁴A. Jennings, X. Zhou, I. Grytsenko, and E. Kawakami, “Quantum computing using floating electrons on cryogenic substrates: Potential and challenges,” *Applied Physics Letters* **124**, 120501 (2024).

⁵D. Schuster, A. Fragner, M. Dykman, S. Lyon, and R. Schoelkopf, “Proposal for manipulating and detecting spin and orbital states of trapped electrons on helium using cavity quantum electrodynamics,” *Physical Review Letters* **105**, 040503 (2010).

⁶A. Blais, A. L. Grimsmo, S. M. Girvin, and A. Wallraff, “Circuit quantum electrodynamics,” *Reviews of Modern Physics* **93**, 025005 (2021).

⁷P. Platzman and M. Dykman, “Quantum computing with electrons floating on liquid helium,” *Science* **284**, 1967–1969 (1999).

⁸T. Kanai, D. Jin, and W. Guo, “Single-electron qubits based on quantum ring states on solid neon surface,” *Physical Review Letters* **132**, 250603 (2024).

⁹X. Li, C. S. Wang, B. Dizdar, Y. Huang, Y. Wen, W. Guo, X. Zhang, X. Han, X. Zhou, and D. Jin, “Noise-resilient solid host for electron qubits above 100 mK,” arXiv:2502.01005v2 (2025).

¹⁰K. Zheng, X. Song, and K. W. Murch, “Surface-morphology-assisted trapping of strongly coupled electron-on-neon charge states,” *Physical Review Letters* **135**, 080601 (2025).

¹¹N. R. Beysengulov, Ø. S. Schøyen, S. D. Bilek, J. B. Flaten, O. Leinonen, M. Hjorth-Jensen, J. Pollanen, H. E. Kristiansen, Z. J. Stewart, J. D. Weidman, *et al.*, “Coulomb interaction-driven entanglement of electrons on helium,” *PRX Quantum* **5**, 030324 (2024).

¹²P. Krantz, M. Kjaergaard, F. Yan, T. P. Orlando, S. Gustavsson, and W. D. Oliver, “A quantum engineer’s guide to superconducting qubits,” *Applied Physics Reviews* **6**, 021318 (2019).

¹³T. Hengsens, T. Fujita, L. Janssen, X. Li, C. Van Diepen, C. Reichl, W. Wegscheider, S. Das Sarma, and L. M. Vandersypen, “Quantum simulation of a fermi–hubbard model using a semiconductor quantum dot array,” *Nature* **548**, 70–73 (2017).

¹⁴Y. Wang, Y. Chen, H. T. Bui, C. Wolf, M. Haze, C. Mier, J. Kim, D.-J. Choi, C. P. Lutz, Y. Bae, *et al.*, “An atomic-scale multi-qubit platform,” *Science* **382**, 87–92 (2023).

¹⁵S. P. Fors, J. Fernández-Pendás, and A. F. Kockum, “Comprehensive explanation of zz coupling in superconducting qubits,” arXiv preprint arXiv:2408.15402 (2024).

¹⁶G. Koolstra, G. Yang, and D. I. Schuster, “Coupling a single electron on superfluid helium to a superconducting resonator,” *Nature communications* **10**, 5323 (2019).

¹⁷S. Poletto, J. M. Gambetta, S. T. Merkel, J. A. Smolin, J. M. Chow, A. Córcoles, G. A. Keefe, M. B. Rothwell, J. Rozen, D. W. Abraham, *et al.*, “Entanglement of two superconducting qubits in a waveguide cavity via monochromatic two-photon excitation,” *Physical Review Letters* **109**, 240505 (2012).

¹⁸C. Rigetti and M. Devoret, “Fully microwave-tunable universal gates in superconducting qubits with linear couplings and fixed transition frequencies,” *Physical Review B* **81**, 134507 (2010).

¹⁹E. Magesan and J. M. Gambetta, “Effective hamiltonian models of the cross-resonance gate,” *Physical Review A* **101**, 052308 (2020).

²⁰J. M. Chow, A. D. Córcoles, J. M. Gambetta, C. Rigetti, B. R. Johnson, J. A. Smolin, J. R. Rozen, G. A. Keefe, M. B. Rothwell, M. B. Ketchen, *et al.*, “Simple all-microwave entangling gate for fixed-frequency superconducting qubits,” *Physical Review Letters* **107**, 080502 (2011).

²¹M. Roth, M. Ganzhorn, N. Moll, S. Philipp, G. Salis, and S. Schmidt, “Analysis of a parametrically driven exchange-type gate and a two-photon excitation gate between superconducting qubits,” *Physical Review A* **96**, 062323 (2017).

²²J. Majer, J. Chow, J. Gambetta, J. Koch, B. Johnson, J. Schreier, L. Frunzio, D. Schuster, A. A. Houck, A. Wallraff, *et al.*, “Coupling superconducting qubits via a cavity bus,” *Nature* **449**, 443–447 (2007).

²³Materials and methods are available as supplementary material.

²⁴J. R. Johansson, P. D. Nation, and F. Nori, “Qutip: An open-source python framework for the dynamics of open quantum systems,” *Computer Physics Communications* **183**, 1760–1772 (2012).

²⁵G. Wendin, “Quantum information processing with superconducting circuits: a review,” *Reports on Progress in Physics* **80**, 106001 (2017).

²⁶J.-k. Xie, R.-t. Cao, Y.-l. Ren, S.-l. Ma, R. Zhang, and F.-l. Li, “High-fidelity quantum memory with floating electrons coupled to superconducting circuits,” *Physical Review A* **110**, 052607 (2024).

²⁷T. A. Baart, T. Fujita, C. Reichl, W. Wegscheider, and L. M. K. Vandersypen, “Coherent spin-exchange via a quantum mediator,” *Nature Nanotechnology* **12**, 26–30 (2017).

²⁸P. Leiderer, “Surface electrons on solid quantum substrates: A brief review,” *Journal of Low Temperature Physics* , 1–20 (2025).

²⁹G. Burkard, T. D. Ladd, A. Pan, J. M. Nichol, and J. R. Petta, “Semiconductor spin qubits,” *Reviews of Modern Physics* **95**, 025003 (2023).

³⁰J. R. Petta, A. C. Johnson, J. M. Taylor, E. A. Laird, A. Yacoby, M. D. Lukin, C. M. Marcus, M. P. Hanson, and A. C. Gossard, “Coherent manipulation of coupled electron spins in semiconductor quantum dots,” *Science* **309**, 2180–2184 (2005).

³¹F. Borsoi, N. W. Hendrickx, V. John, M. Meyer, S. Motz, F. Van Riggelen, A. Sammak, S. L. DeSnoo, G. Scappucci, and M. Veldhorst, “Shared control of a 16 semiconductor quantum dot crossbar array,” *Nature Nanotechnology* **19**, 21–27 (2024).

³²L. Vandersypen, H. Bluhm, J. Clarke, A. Dzurak, R. Ishihara, A. Morello, D. Reilly, L. Schreiber, and M. Veldhorst, “Interfacing spin qubits in quantum dots and donors—hot, dense, and coherent,” *npj Quantum Information* **3**, 34 (2017).

³³A. Zwerger, T. Krähenmann, T. Watson, L. Lampert, H. C. George, R. Pillarisetty, S. Bojarski, P. Amin, S. Amitonov, J. Boter, *et al.*, “Qubits made by advanced semiconductor manufacturing,” *Nature Electronics* **5**, 184–190 (2022).

³⁴J. Dijkema, X. Xue, P. Harvey-Collard, M. Rimbach-Russ, S. L. deSnoo, G. Zheng, A. Sammak, G. Scappucci, and L. M. Vandersypen, “Cavity-mediated iswap oscillations between distant spins,” *Nature Physics* **21**, 168–174 (2025).

³⁵L. Cheung, R. Haller, A. Kononov, C. Ciaccia, J. Ungerer, T. Kanne, J. Nygård, P. Winkel, T. Reisinger, I. Pop, *et al.*, “Photon-mediated long-range coupling of two andreev pair qubits,” *Nature Physics* **20**, 1793–1797 (2024).

³⁶C. Bottcher, S. Harvey, S. Fallahi, G. Gardner, M. Manfra, U. Vool, S. Bartlett, and A. Yacoby, “Parametric longitudinal coupling between a high-impedance superconducting resonator and a semiconductor quantum dot singlet-triplet spin qubit,” *Nature Communications* **13**, 4773 (2022).

³⁷P. Harvey-Collard, G. Zheng, J. Dijkema, N. Samkharadze, A. Sammak, G. Scappucci, and L. M. Vandersypen, “On-chip microwave filters for high-impedance resonators with gate-defined quantum dots,” *Physical Review Applied* **14**, 034025 (2020).

³⁸P. Harvey-Collard, J. Dijkema, G. Zheng, A. Sammak, G. Scappucci, and L. M. Vandersypen, “Coherent spin-spin coupling mediated by virtual microwave photons,” *Physical Review X* **12**, 021026 (2022).

³⁹A. Stockklauser, P. Scarlino, J. V. Koski, S. Gasparinetti, C. K. Andersen, C. Reichl, W. Wegscheider, T. Ihn, K. Ensslin, and A. Wallraff, “Strong coupling cavity qed with gate-defined double quantum dots enabled by a high impedance resonator,” *Physical Review X* **7**, 011030 (2017).

⁴⁰A. J. Landig, J. V. Koski, P. Scarlino, C. Müller, J. C. Abadillo-Uriel, B. Kratochwil, C. Reichl, W. Wegscheider, S. N. Coppersmith, M. Friesen, *et al.*, “Virtual-photon-mediated spin-qubit-transmon coupling,” *Nature communications* **10**, 5037 (2019).

⁴¹G. Koolstra, E. Glen, N. Beysengulov, H. Byeon, K. Castoria, M. Sammon, B. Dizdar, C. Wang, D. Schuster, S. Lyon, *et al.*, “High-impedance resonators for strong coupling to an electron on helium,” *Physical Review Applied* **23**, 024001 (2025).

⁴²Y. Tian, I. Grytsenko, A. Jennings, J. Wang, H. Ikegami, X. Zhou, S. Tamate, H. Terai, H. Kutsuwa, D. Jin, *et al.*, “Nb_{tin} nanowire resonators for spin-photon coupling on solid neon,” arXiv preprint arXiv:2505.24303 (2025).

⁴³X.-F. Pan and P.-B. Li, “Nonlinear tripartite coupling of single electrons on solid neon with magnons in a hybrid quantum system,” arXiv preprint arXiv:2503.08587 (2025).

Supplementary Information for Coherent manipulation of interacting electron qubits on solid neon

A. Devices and experiments

The data presented in Fig. 2 and Fig. 3 were collected on a high-impedance titanium nitride (TiN) splitting superconducting resonator, the same as the one in ref. ⁹. The resonator supports a differential mode at 5.668 GHz with a total linewidth of $\kappa/2\pi = 0.38$ MHz. Electrodes with on-chip low-pass filters are connected to the resonator pins and trap guards surrounding the electron-trapping area to apply bias voltages for tuning qubits transition frequency. The device was mounted on a home-made printed circuit board (PCB), sealed in a copper cell with neon filling lines, tungsten filaments, and electrical connectors on top of the cell lid. The cryogenic and room temperature electronics setups are the same as those in ref. ⁹. The data presented in Fig. 4 were collected on a niobium splitting superconducting resonator, the same as the one in refs. ^{1,2}. This resonator supports a differential mode at 6.426 GHz, with a total linewidth of $\kappa/2\pi = 0.46$ MHz. The sample mounting, cryogenic and room temperature electronic setups were the same as those in refs. ^{1,2}.

The neon growth procedure is the same as that described in ref. ⁹. In summary, the dilution fridge is warmed up to create a temperature gradient from ~ 27 K to ~ 25 K between its 4K plate and mixing chamber (MXC) plate. At that moment, neon gas is supplied from a room-temperature gas handling system in the form of puffs and filled onto the device chip in the form of liquid. After a desired amount of neon filling, the fridge heater is turned off to let the fridge cool down to base temperature.

Electrons are deposited on to the chip by sending pulsed current on to the tungsten filaments mounted above the device chip. During the electron firing process, temperature sensed on the MXC plate can increase up to 100 mK. The details of the procedure and discussion of the electron deposition process can be found in ref. ⁹.

B. Simulation of multi-qubit coupled systems

The populations of qubits in coupled systems are simulated based on their Hamiltonian, using the QUTiP package ²⁴. For the numerical data presented in Fig. 3, we use Eq. 1 to Eq. 5 as the Hamiltonian, with parameters listed in the following sections and Tab. S1. The Lindblad master equation is applied to model the effects of relaxation and dephasing:

$$\begin{aligned} \frac{d\hat{\rho}}{dt} = & -\frac{i}{\hbar}[\hat{H}, \hat{\rho}] \\ & + \frac{\kappa}{2}(2\hat{a}\hat{\rho}\hat{a}^\dagger - \hat{a}^\dagger\hat{a}\hat{\rho} - \hat{\rho}\hat{a}^\dagger\hat{a}) \\ & + \sum_i \frac{\Gamma_i}{2}(2\hat{\sigma}_i^- \hat{\rho}\hat{\sigma}_i^+ - \hat{\sigma}_i^+ \hat{\sigma}_i^- \hat{\rho} - \hat{\rho}\hat{\sigma}_i^+ \hat{\sigma}_i^-) \\ & + \sum_i \frac{\Gamma_i^\varphi}{2}(2\hat{\sigma}_i^+ \hat{\sigma}_i^- \hat{\rho}\hat{\sigma}_i^+ \hat{\sigma}_i^- - (\hat{\sigma}_i^+ \hat{\sigma}_i^-)^2 \hat{\rho} - \hat{\rho}(\hat{\sigma}_i^+ \hat{\sigma}_i^-)^2), \end{aligned} \quad (\text{S1})$$

where $\hat{H} = \hat{H}_{\text{sys}} + \hat{H}_{\text{dr}}$. $\hat{\rho}$ is the system density matrix. $1/\Gamma_i$ is the relaxation lifetime T_1 of Q_i , and $2/\Gamma_i^\varphi$ is the pure dephasing lifetime T_φ of Q_i , which are adopted from relaxation and Ramsey measurements in Fig. S3.

To simulate the system under driving pulses starting at time $t = 0$ with a time-dependent amplitude $A(t)$ and frequency ω_{dr} , the driving Hamiltonian can be written as

$$\hat{H}_{\text{dr}} = A(t)\cos(t\omega_{\text{dr}}) \sum_i \hbar\eta_i(\hat{\sigma}_i^+ + \hat{\sigma}_i^-), \quad (\text{S2})$$

where $\eta_i \propto g_i$ is the ratio for direct driving on Q_i (ref. ¹⁷). In the two-qubit system discussed in the main text $\eta_b \sim 1$ and $\eta_d \sim 0$. The numerical simulation is performed in the rotating frame at the drive frequency.

To simulate the readout process, we introduce the Hamiltonian of the probing at the resonator (\hat{H}_{p}) to the system Hamiltonian in the rotating frame as:

$$\hat{H}_{\text{p}} = \epsilon\hbar(\hat{a}^\dagger + \hat{a}), \quad (\text{S3})$$

where ϵ is the probing amplitude.

C. Resonator dispersive shift

Q_b of the two-qubit coupled system presented in the main text is coupled to the resonator with its charge sweet-spot (SS) above the resonator frequency. Due to the interaction, the resonator is dispersively shifted when Q_b is biased close to its SS, as shown in Fig. S1A. The line-cut of the resonator spectrum when ground-state Q_b is on its SS shows $\chi/2\pi = 0.33$ MHz red shift compared to the bare resonator frequency, as shown in Fig. S1B. We estimated the coupling strength between Q_b and resonator to be $g_b/2\pi \approx 3.76$ MHz based on this resonator dispersive shift and $\chi \approx g_b^2/\Delta_b$ (ref. ⁶), where $\Delta_b/2\pi = (\omega_b - \omega_r)/2\pi \approx 43$ MHz.

D. Pulsed readout of Q_d

We demonstrate the pulsed readout process of Q_d with the following simulation. Initially, the population of Q_b and Q_d is set to be 0 and 1, respectively. Then the resonator is populated by sending a square readout pulse (700 ns) at the resonator frequency with varying amplitude ϵ . The evolution of the coupled system is calculated with the system Hamiltonian Eq. 1 and the probing Hamiltonian Eq. S3, considering relaxation and dephasing with Eq. S1.

Figure S2 shows the evolution of intra-cavity photon number \bar{n} , Q_b , and Q_d excited state population under varying driving amplitude. When the probe power is small (Fig. S2A and Fig. S2B), the ac-Stark shift of Q_b caused by the probe pulse is also small, Q_b and Q_d weakly exchange population at high frequency approximately $\sqrt{\Delta_{bd}^2 + 4J^2}$, where J is the inter-qubit coupling strength and Δ_{bd} are the qubits detune. With increased photon number, the blue ac-Stark shift $2\chi\bar{n}$ causes the Q_b across Q_d frequency, resulting in their population swap when \bar{n} approaches 20, as shown in Fig. S2C. Further increasing the probing amplitude could populate the resonator faster and make the population swap happen even sooner. These simulation results reveal the readout process we applied to probe Q_d , whose direct interaction strength with the resonator is negligible. We chose the 700 ns readout length to balance signal strength with the fast decaying of Q_b , as illustrated in the qubit decoherence section.

E. Qubits decoherence

We evaluated Q_b and Q_d 's coherence via relaxation and Ramsey measurements when Q_b was biased at its SS. Q_b was directly driven by sending pumps through the resonator at its frequency. In contrast, Q_d was driven by pumping Q_b at Q_d 's frequency, corresponding to the cross-resonance two-qubit operation. Q_d was probed with the pulsed readout method described in the main text and the previous sections. Figure S3A and S3B show the relaxation of Q_b and Q_d with T_1 of 1.8 μ s and 30.3 μ s, respectively, fitted from the measured in-phase signal. Figure S3C shows the Ramsey fringes of Q_b , with a T_2^* of 2.56 μ s fitted from the in-phase signal. The Ramsey measurement result of Q_d is more complicated, as we observed multiple frequency components of the measured in-phase signal, as shown in Fig. S3D and S3E. Numerical simulation of the Ramsey measurement process with a stable single frequency of Q_d reveals that the population swap between Q_b and Q_d induced by the inter-qubit coupling will not affect the final probed state and measured signal. Therefore, we attribute the beating features in Fig. S3D to fluctuations of the Q_d 's frequency during data acquisition, which has also occurred on other qubits measured on the same device, as presented in ref. ⁹. We fitted the data in Fig. S3D with a three-frequency model, which resulted in a T_2^* of 32.99 μ s. The measured relaxation and decoherence rates are then used in the numerical simulation of the system, as shown in Tab. S1.

F. Numerical simulation parameters

Table S1 summarizes the simulation parameters to build the Hamiltonian of the two-qubit coupled system and to account for the decoherence. Since the longitudinal interaction is small, as discussed in the main text, ZZ coupling is excluded in the simulation. The resonator has a frequency of 5.668 GHz with linewidth $\kappa/2\pi = 0.38$ MHz. The interaction strength between the bright qubit and the resonator is $g_b/2\pi = 3.76$ MHz. In addition, the driving amplitude A in MHz used in the simulation is scaled with $A = 735 \times \mathcal{A}$, where \mathcal{A} is the experimental driving pulse amplitude in V . The readout process is simulated with 700 ns square pulse with probing amplitude ϵ at 18 MHz.

Figure S4 shows the simulated qubit excited state population before the readout process in the Rabi measurements, indicated as the arrow time stamp in the inset. The oscillation features at 5.726 GHz and 5.718 GHz, corresponding to the cross-resonance (CR) and bSWAP operation, match well with the experimental result in Fig. 3 of the main text. It confirms that the observed oscillation features are the result of the two-qubit operations instead of the probing

pulse following that. In Fig. S4A and S4C, when Q_d is excited by driving Q_b at 5.726 GHz, the Q_b 's population barely changes. After the readout process, the Q_d 's population is swapped onto Q_b , as shown in Fig. 3B and 3D of the main text.

To calculate the eigenstates of the three-qubit coupled system, as in the main text Fig. 4, we modeled qubits 1, 2, and 3 with hyperbolic frequency dependency on the gate voltage ΔV_{res} as: $f_i = \sqrt{(\alpha_i)^2 + (\beta_i \times (\Delta V_{\text{res}} - \delta_i))^2}$. In Tab. S2, we list the parameters used to generate Fig. 4C in the main text. In addition, we used $J_{12}/2\pi = 62.5$ MHz and $J_{23}/2\pi = 5.0$ MHz. We also omit longitudinal interactions between qubits in this calculation.

G. “Waterfall” features in pulse amplitude-dependent Rabi oscillation

The “waterfall-like” pattern measured in pulse amplitude-dependent Rabi oscillation is also replicated in the numerical simulation, by realistically modeling the driving pulse with the same Gaussian envelope used in experiments. We attribute it to the combined effects of the pulse shape and ac-Stark shift of Q_b under driving at the frequency middle point between Q_b and Q_d with high power. Figure S5 plots the simulation when we replace the Gaussian-shaped driving pulse with square pulses. Under such conditions, the “waterfall-like” pattern vanishes while we could still observe the red shift of the $|0_b 0_d\rangle \rightarrow |1_b 1_d\rangle$ transition at higher power, caused by the ac-Stark shift of Q_b .

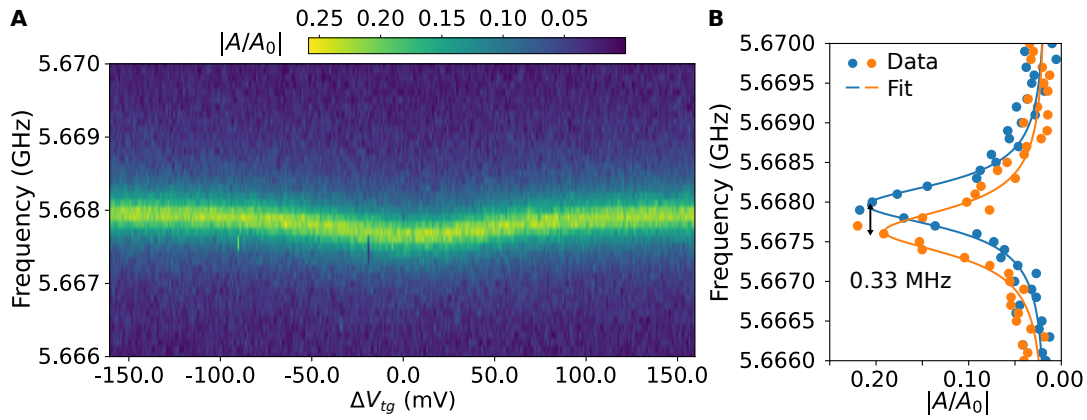


Fig. S1. Resonator dispersive shift caused by Q_b . (A) Resonator spectrum probe with varying bias on trap guard, showing the dispersive shift when Q_b is close to resonator frequency. (B) Transmission line cuts at bare resonator (blue dots and curve) and when Q_b is biased at its sweet-spot (orange dots and curve).

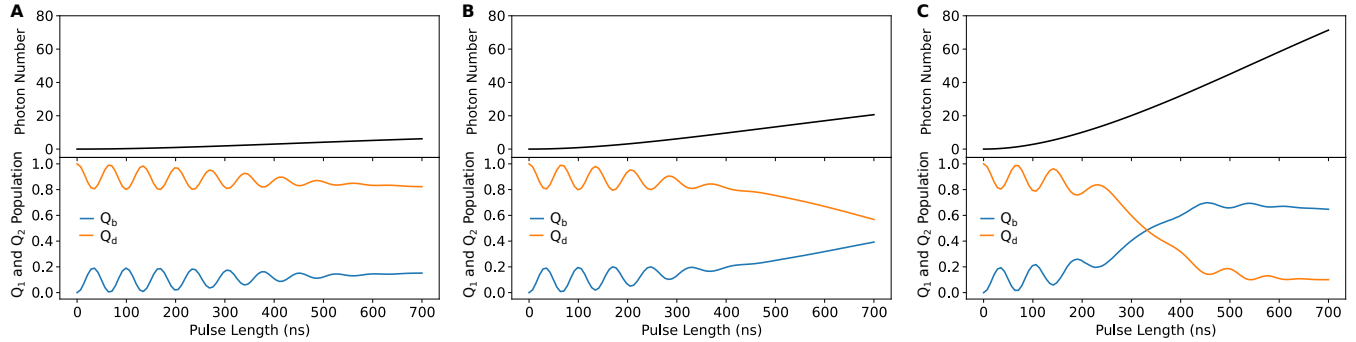


Fig. S2. Simulation of intra-cavity photon number and qubit population evolution with varying probing amplitude. 700 ns evolution simulated with probing amplitude ϵ of (A) 5.6 MHz (-130 dBm reaching the resonator), (B) 10 MHz (-125 dBm reaching the resonator) and (C) 18 MHz (-120 dBm reaching the resonator), respectively. Black curves show intra-cavity photon number \bar{n} . Blue curves show Q_b population and orange curves show Q_d population.

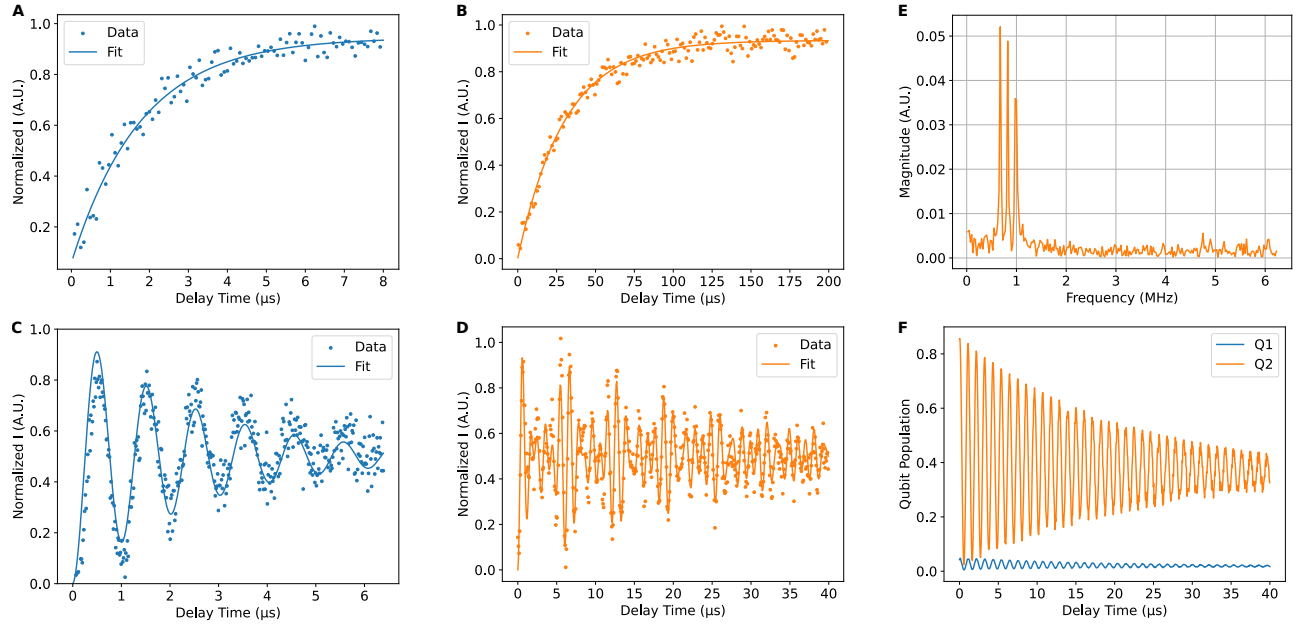


Fig. S3. Relaxation and decoherence of Q_b and Q_d . (A) and (B) Relaxation measurements of Q_b (A) and Q_d (B) with fitted T_1 of $1.8\ \mu\text{s}$ and $30.3\ \mu\text{s}$, respectively. (C) and (D) Ramsey measurements of Q_b (C) and Q_d (D) with fitted T_2^* of $2.56\ \mu\text{s}$ and $32.99\ \mu\text{s}$, respectively. (E) Frequency components of the Ramsey fringes in (D), revealing frequency fluctuations of Q_d during the measurement. (F) Numerical simulation of Ramsey measurement of Q_d , indicating that the beating pattern in (C) is not intrinsically caused by the coupled system.

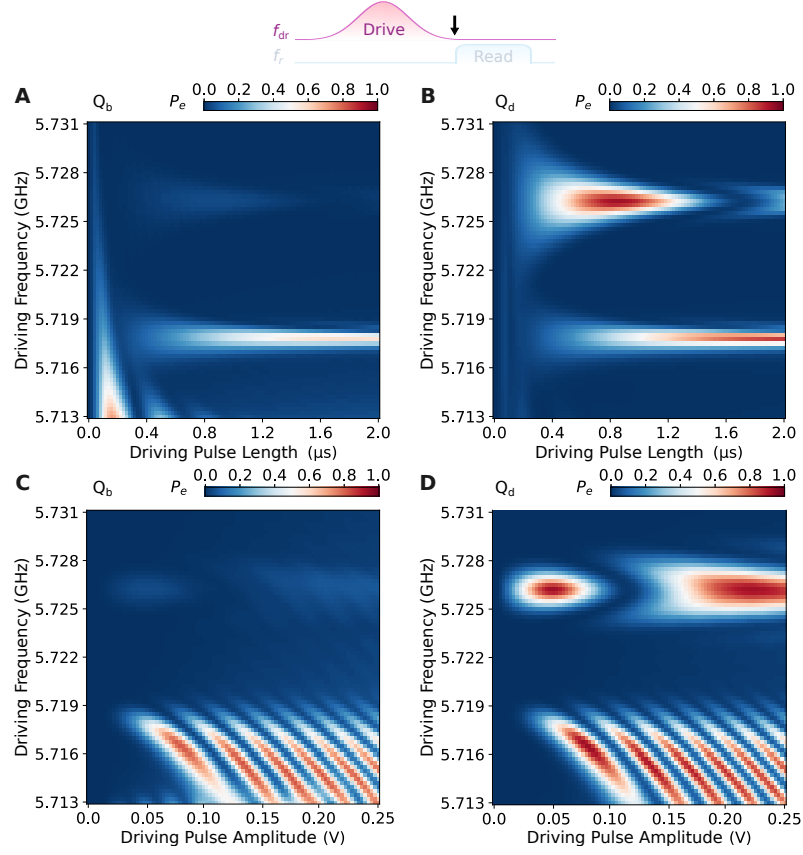


Fig. S4. Numerical simulation of qubit excited state population before the readout process in Rabi measurements. (A) and (B) Simulation results of Q_b (A) and Q_d (B) population after driving pulse in the pulse length-frequency Rabi measurements. (C) and (D) Simulation results of Q_b (C) and Q_d (D) population after driving pulse in the pulse amplitude-frequency Rabi measurements.

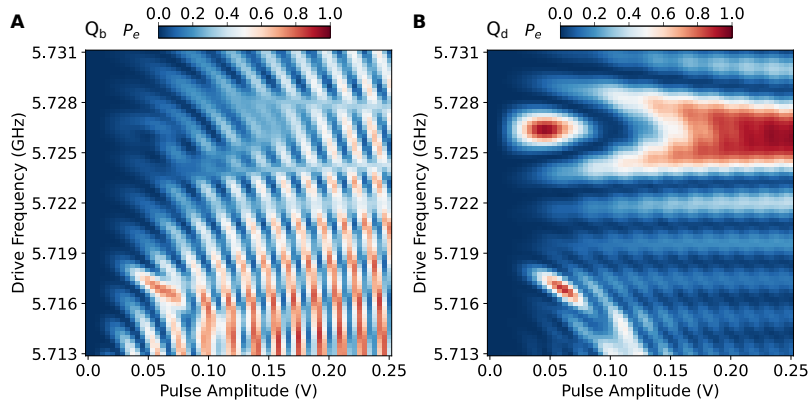


Fig. S5. Numerical simulation of pulse amplitude-dependent Rabi oscillation with step driving pulses. Simulation results of Q_b (A) and Q_d (B) population evolution, in which the “waterfall-like” pattern observed in experiments vanishes.

Tab. S1. Summary of the qubit parameters used for simulating the two-qubit coupled system as in Fig. 3 and Fig. S4.

	$\omega_i/2\pi$ (GHz)	$\Gamma_i/2\pi$ (MHz)	$\Gamma_i^\varphi/2\pi$ (MHz)	$g_i/2\pi$ (MHz)	$J/2\pi$ (MHz)
Bright Q _b	5.7112	0.088	0.036	3.76	
Dark Q _d	5.7255	0.0053	0.0044	0.0	

Tab. S2. Summary of the qubit parameters used for modeling the three-qubit coupled system as in Fig. 4C of the main text.

	α_i (GHz)	β_i (GHz/mV)	δ_i (mV)
Qubit 1	6.130	1.325	0.0
Qubit 2	6.135	0.218	-4.0
Qubit 3	5.915	1.30	0.08